J. Fluid Mech. (1996), *vol.* 308, *pp.* 363–379

Supersonic cooling by shock–vortex interaction

By M. D. FOX† AND M. KUROSAKA
Department of Aeronautics and Astronautics, University of Washington, Seattle, WA 98195-2400, USA

(Received 11 July 1994 and in revised form 21 September 1994)

The subject of total temperature separation in jets was treated in Fox *et al.* (1993) for subsonic jets. When we extended this study to the case of supersonic jets, we found the presence of a different mechanism of cooling, an effect which does not appear to have been known in the past. Named the 'shock-induced total temperature separation', this cooling can be of much greater magnitude than the subsonic cooling treated previously; it is caused by the interaction of convected vortical structures near the jet exhaust with the shock structure of the supersonic jet.

In studying this phenomenon, we focus our attention on overexpanded jets exiting a convergent–divergent nozzle. The theoretical results for the shock-induced cooling which are based on a linearized, unsteady supersonic analysis are shown to agree favourably with experiments.

When an impingement plate is inserted, the shock-induced cooling would manifest itself as wall cooling, whose magnitude is significantly larger than the subsonic counterpart. This has implications for heat transfer not only in jets, but wherever vortical structures may interact with shock waves.

1. Introduction

In our preceding paper (Fox *et al.* 1993, hereafter referred to as Part 1: note that figure 6 of this was omitted in print, and later appeared in a corrigendum), we discussed the general subject of total temperature separation in vortex-dominated flows and applied it to jet flows in particular. This investigation was conducted in pursuit of the theme of vortex-induced total temperature separation, an earlier example of which had been presented for a wake flow (Kurosaka *et al.* 1987; Ng, Chakroun & Kurosaka 1990). Specifically, in Part 1 we have shown that for a free jet, vortex rings around the jet separate the total temperature into two coannular regions: a region of higher total temperature on the inside of the jet and a region of lower total temperature towards the jet periphery. For an impinging jet, we furthermore showed that for small distances of the impingement plate from the nozzle, secondary vortical structures are formed on the plate by an unsteady separation of the boundary layer. This in turn induces secondary total temperature separation and causes a significant reduction in the adiabatic wall temperature. For a heated, thermally conducting plate, this translates to an increase in the local heat transfer rate.

The jets treated in Part 1 were all subsonic and emanated from a convergent nozzle; it was observed that the magnitude of this separation in the total temperature scales with the square of the jet Mach number, as expected. We thought, unsuspectingly, that when jets became supersonic, essentially the same pattern of total temperature separation as for the subsonic jets would continue.

† Present address: Solar Turbines Inc., San Diego, CA 92186-5376, USA.

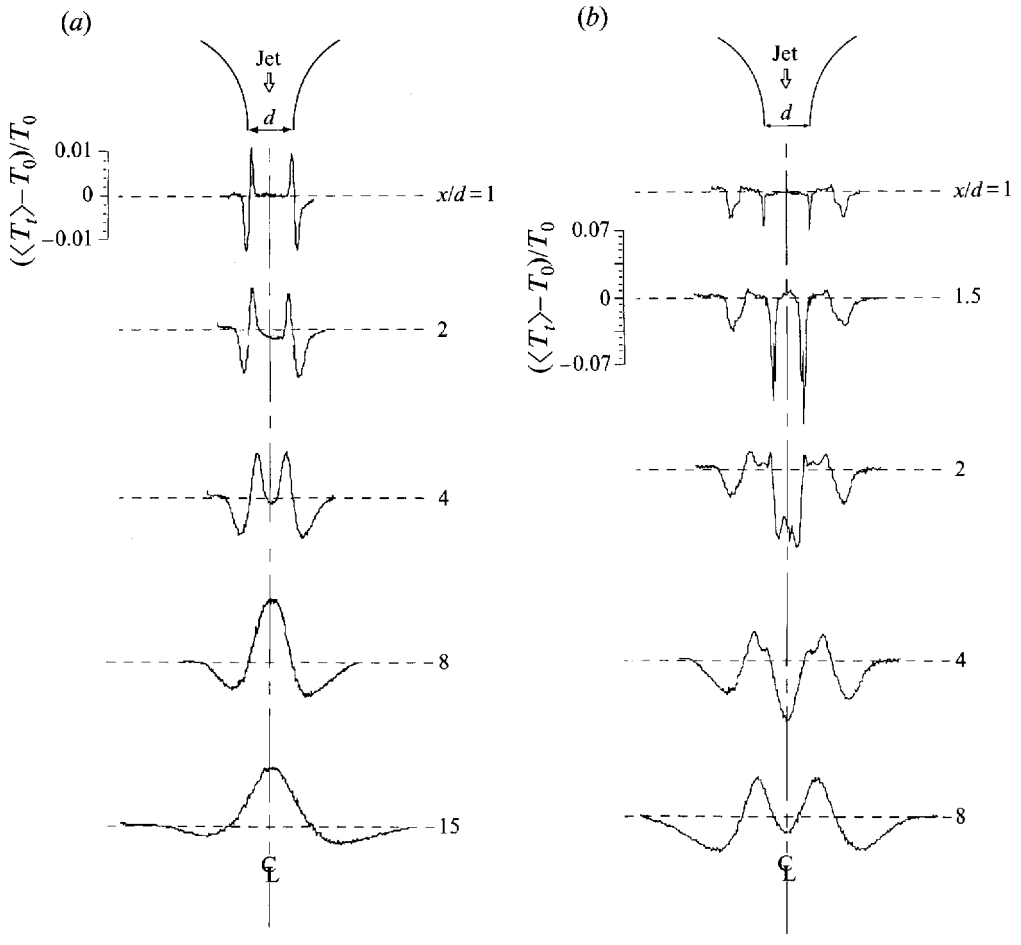

FIGURE 1. (*a*) Measured total temperature profiles for a subsonic free jet. The pressure ratio of 1.7 corresponds to a Mach number of 0.9. (*b*) Corresponding data for the underexpanded jet with a pressure ratio of 7.8.

When a circular convergent nozzle of 2.5 cm diameter is used to produce an underexpanded jet, however, the results are noticeably different. Figure 1 displays a comparison between the time-averaged total temperature distributions $\langle T_t \rangle$ for two free jets: (*a*) for a highly subsonic jet ($P_0/P_a = 1.7$, where P_0 is the reservoir total pressure and P_a is the ambient pressure; note that the critical pressure ratio is 1.89); and (*b*) an underexpanded supersonic jet ($P_0/P_a = 7.8$). (During the tests, the total temperature of the jet as measured in the upstream settling chamber, T_0, is held constant and equal to the ambient temperature, $T_a = 21$ °C.) The radial profiles of the total temperature are plotted at several locations, x/d, where x is the downstream distance from the nozzle and d is the nozzle diameter.

For the subsonic jet (figure 1*a*), the presence of inner peaks and outer valleys in the profile in the near field corresponds to the aforementioned vortex-induced separation. The coalescence of the twin peaks into a single peak in the far field is caused by the entrainment of ambient fluid into the jet, which is also discussed in detail in Part 1. Contrast these subsonic data with the underexpanded supersonic data (figure 1*b*). We start from the near field at $x/d = 1$: the outer valleys of lowered T_t correspond to the subsonic mechanism. However, the adjacent inner peaks of heating observed for a

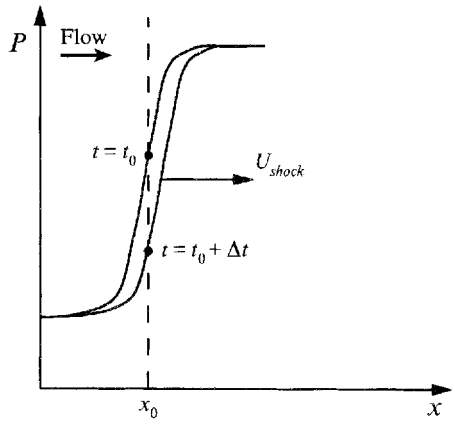

FIGURE 2. Mechanism of cooling across a shock.

subsonic jet are now almost suppressed; instead additional, sharp valleys of cooling occur at a slightly smaller radial distance from the centreline. As we move further from the nozzle, these inboard valleys move closer to the jet centreline and grow in magnitude; at $x/d = 1.5$ this cooling is more than 35 °C (i.e. the minimum total temperature is 35 °C lower than the ambient temperature), much greater than that due to the vortex-induced cooling. At $x/d = 2$, they coalesce and form a single valley of cooling on the centreline, which persists further downstream, and the peaks of heating start to emerge.

In search of a proper explanation for these unexpected features of supersonic jets, which initially baffled us, we were led to a second mechanism of total temperature separation unique to a supersonic flow: vortex–shock interaction or the movement of the shock caused by the formation and movement of vortices. This is the subject of the present paper.

In general, as is well known, the total temperatures across a moving shock are not the same, as is evident from a coordinate transformation between stationary and moving coordinate systems. What may be perhaps not so well known is that the conclusion about the difference in total temperatures can also be obtained from a dynamical argument by appealing to the following equation used in Part 1 as a key for subsonic vortex-induced T_t separation:

$$C_p \frac{\mathrm{D}T_t}{\mathrm{D}t} = \frac{1}{\rho} \frac{\partial p}{\partial t}. \tag{1}$$

Consider, for simplicity, a normal shock, the pressure rise across which is shown schematically in figure 2 at two different times (here the shock thickness is deliberately broadened so that the pressure rise can appear as a continuous curve). The shock begins to move at time $t = t_0$, and has moved a small distance downstream by a time $t = t_0 + \Delta t$. For a fluid particle momentarily occupying the position x_0, $\partial p/\partial t < 0$ and T_t decreases along its pathline as the shock moves downstream.

Returning to the present case of a supersonic jet, we can expect that every time a vortical structure moves downstream, it disrupts the shocks and sets them in motion: this could lead to a change in total temperature. Crudely speaking, then, this is the heart of the mechanism of total temperature change in a supersonic jet, where equation (1) serves as a common thread between this new mechanism and the subsonic counterpart treated in Part 1. To distinguish these two mechanisms, the mechanism of

Part 1 will be called simply *vortex-induced T_t separation*: T_t separation is induced either by the rotary motion of fluid particles entrapped around vortices or by those particles entrained into the jet by vortices. The present mechanism for supersonic flows will be called *shock-induced T_t separation*.

Needless to say, further details have to be added to the above broad-brush description in order to be able to answer various questions. In particular, two questions stand out. (i) Why does such shock–vortex interaction lead, when time-averaged, only to cooling? And (ii) why do the secondary valleys near the jet centreline of figure 1(*b*), which are postulated to correspond to shock-induced cooling, move radially inward as the distance from the nozzle increases?

In what follows, we address these issues. In §2, we offer an analysis based on a linearized unsteady supersonic approximation, where the roots of the leading shocks are fixed at the nozzle outlet. This corresponds to the near field of a convergent–divergent nozzle operated at an overexpanded condition. In §3, comparison will be made with total temperature profiles measured for overexpanded free jets emanating from a convergent–divergent nozzle, which will display features similar to figure 1(*b*) for the convergent nozzle. The results of the analysis, though obviously idealized, seem to agree favourably with the experimental trends; this appears to lend support to the hypotheses adopted in the course of analysis.

2. A model problem for shock movement induced by vortices

The objective of the model problem is to analyse the shock-induced T_t change which is caused by the movement of an oblique shock. The shock is set in motion by the generation, and subsequent convection, of vortices.

As sketched in figure 3, we are interested in the motion of an oblique shock, which, in its undisturbed state, emanates from a point at the nozzle outlet, A: $x = 0$ and $r = a$, where x is the axial and r is the radial coordinate. The following simplifying assumptions are to be made.

(i) A boundary condition is imposed at $r = a$ as a specified radial component of the velocity. It is subsequently chosen in such a way that the effect of the vortices is represented as an appropriate time-varying pressure drop. As a consequence of prescribing the boundary condition at $r = a$, the interior region of $r \leqslant a$, the domain of interest, is separated from $r > a$ and the interior is rendered to a 'duct' problem.

(ii) The flow in the nozzle, which is located upstream of the leading oblique shock, remains undisturbed, uniform, and constant.

(iii) Downstream of the leading oblique shock, we employ linearized, unsteady and irrotational supersonic analysis and apply its results near the leading shock wave as an input to obtain the shock motion; for simplicity, and as justified in §2.4, we treat the disturbance as axisymmetric. From this, we calculate the shock-induced T_t change. (Here we ignore the vortex-induced T_t change of §1, which is the mechanism dealt with in Part 1.)

(iv) In general, any unsteady disturbance generates a vortical flow field and entropy in addition to irrotational flow. Although in the linearized treatment all three are formally decoupled in such a way that vorticity and entropy drift with the stream, and the irrotational disturbance satisfies the convected wave equation, they are coupled at the shock. For a weak shock, however, the entropy and vortical flow field are of higher order. If we denote the steady strength of a base weak shock by ϵ and the amplitude of the unsteady disturbance by θ_0, then the entropy disturbance is $O(\epsilon^2\theta_0)$; for an oscillating wedge, where a complete solution is available (Carrier 1949), a detailed

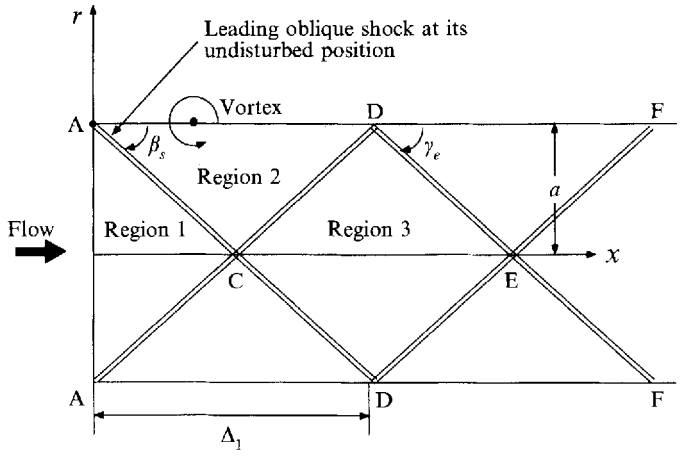

FIGURE 3. Schematic of the model problem of §2.

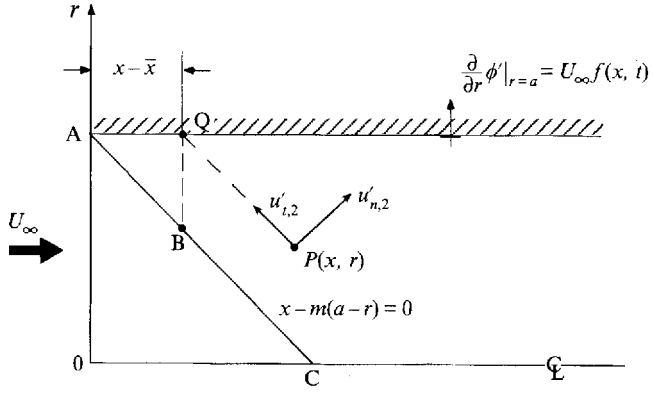

FIGURE 4. Detail of the notation for the model problem of §2.

study shows that the rotational component of the flow is $O(\epsilon^{3/2}\theta_0)$ (Kurosaka 1977). Thus, to the order of present interest, $O(\theta_0)$, the irrotational approximation suffices.

2.1. *Linearized unsteady analysis downstream of the shock*

The governing equation for the perturbed velocity potential ϕ' is given by

$$-m^2\frac{\partial^2}{\partial x^2}\phi' + \frac{\partial^2}{\partial r^2}\phi' + \frac{1}{r}\frac{\partial}{\partial r}\phi' - 2\frac{M_\infty}{a_\infty}\frac{\partial^2}{\partial x\,\partial t}\phi' - \frac{1}{a_\infty^2}\frac{\partial^2}{\partial t^2}\phi' = 0, \tag{2}$$

where t is the time, $m = (M_\infty^2 - 1)^{1/2}$, $M_\infty = U_\infty/a_\infty$,

U_∞ and a_∞ are the upstream free-stream and acoustic velocities, respectively.

The boundary conditions are

$$\frac{\partial}{\partial r}\phi' = U_\infty f(x,t) \quad \text{at} \quad r = a, \tag{3}$$

where $f(x, t)$ is an arbitrary function of $O(\theta_0)$, which vanishes for $x < 0$. Upstream of the leading Mach wave emanating from point A (see figure 4),

$$\phi' = 0, \quad x - m(a-r) < 0, \tag{4}$$

and hereafter our attention is focused on the upper half of the 'duct'.

We apply the Fourier transform in t and then the Laplace transform in x, using the Fourier transform defined by

$$\hat{\phi} = \frac{1}{(2\pi)^{1/2}} \int_{-\infty}^{\infty} \phi' \, \mathrm{e}^{-\mathrm{i}\omega t} \, \mathrm{d}t,$$

and the Laplace transform defined by

$$\tilde{\phi} = \int_0^{\infty} \hat{\phi} \, \mathrm{e}^{-sx} \, \mathrm{d}x.$$

Then equations (2) and (3) become

$$\frac{\mathrm{d}^2}{\mathrm{d}r^2}\tilde{\phi} + \frac{1}{r}\frac{\mathrm{d}}{\mathrm{d}r}\tilde{\phi} - m^2(s+\alpha)(s+\beta)\tilde{\phi} = 0, \tag{5}$$

where $$\alpha = \frac{\mathrm{i}\omega}{a_\infty m^2}(M_\infty - 1) \quad \text{and} \quad \beta = \frac{\mathrm{i}\omega}{a_\infty m^2}(M_\infty + 1),$$

and $$\frac{\partial}{\partial r}\tilde{\phi} = U_\infty \tilde{f} \quad \text{at} \quad r = a. \tag{6}$$

A solution of (5) subject to (6) is given by

$$\tilde{\phi} = U_\infty \frac{\tilde{f}}{m} \frac{I_0\{rm[(s+\alpha)(s+\beta)]^{1/2}\}}{[(s+\alpha)(s+\beta)]^{1/2} I_1\{am[(s+\alpha)(s+\beta)]^{1/2}\}}, \tag{7}$$

where I_0 and I_1 are modified Bessel functions. For large values of s, which correspond to small values of x, the asymptotic form of I for $r \neq 0$ yields

$$\tilde{\phi} = \frac{U_\infty f}{m} \frac{1}{[(s+\alpha)(s+\beta)]^{1/2}} \left(\frac{a}{r}\right)^{1/2} \exp\{-m(a-r)[(s+\alpha)(s+\beta)]^{1/2}\}.$$

By convolution, this may be inverted as

$$\hat{\phi} = \frac{U_\infty}{m}\left(\frac{a}{r}\right)^{1/2} \int_0^{x-\bar{x}} \hat{f} \exp\left[-\frac{\mathrm{i}\omega M_\infty}{a_\infty m^2}(x-\xi)\right] J_0\left[\frac{\omega}{a_\infty m^2}[(x-\xi)^2 - m^2(a-r)^2]^{1/2}\right] \mathrm{d}\xi, \tag{8}$$

where $\hat{f}$ is the Laplace transform of f, J_0 is a Bessel function, and

$$\bar{x} = m(a-r). \tag{9}$$

In deriving the above, use is made of the fact that the inverse Laplace transform of

$$\frac{\exp\{-\gamma[(s+\alpha)(s+\beta)]^{1/2}\}}{[(s+\alpha)(s+\beta)]^{1/2}}$$

is given (e.g. Erdelyi 1954) as

$$H(x-\gamma)\exp[-\tfrac{1}{2}(\alpha+\beta)x] I_0[\tfrac{1}{2}(\alpha-\beta)(x^2-\gamma^2)^{1/2}],$$

where H is the step function. By taking the inverse Fourier transform of (8), one obtains

$$\phi' = \frac{U_\infty}{\pi m}\left(\frac{a}{r}\right)^{1/2} \int_0^{x-\bar{x}} \mathrm{d}\xi \int_{-\infty}^{\infty} f(\xi,\tau) \frac{H(\sigma)}{[(\tau-\tau_1)(\tau_2-\tau)]^{1/2}} \mathrm{d}\tau, \tag{10}$$

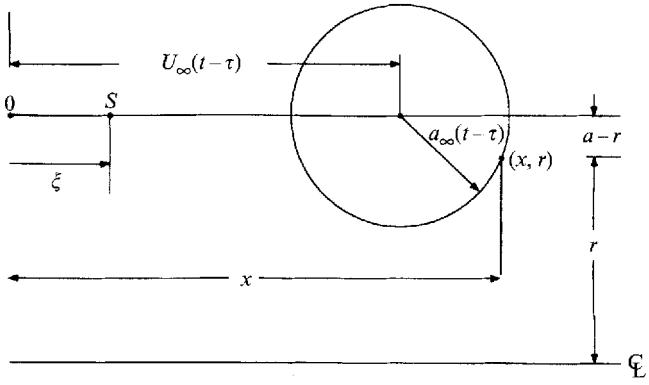

FIGURE 5. Diagram of a propagating signal from a convected source.

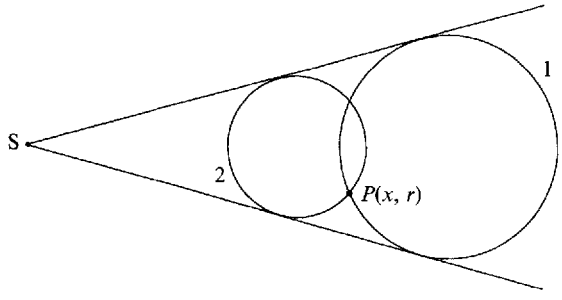

FIGURE 6. Schematic of the zone of influence of signals from a source at point S. Wavelet 1 originated at point S at time τ_1 and wavelet 2 originated at point S at time τ_2.

where
$$\sigma = \frac{1}{a_\infty m^2}[(x-\xi)^2 - m^2(a-r)^2]^{1/2} - \left| t-\tau-\frac{M_\infty}{a_\infty m^2}(x-\xi)\right|, \tag{11a}$$

$$\tau_2 = t-\frac{1}{a_\infty m^2}\{M_\infty(x-\xi)-[(x-\xi)^2-m^2(a-r)^2]^{1/2}\}, \tag{11b}$$

and
$$\tau_1 = t-\frac{1}{a_\infty m^2}\{M_\infty(x-\xi)+[(x-\xi)^2-m^2(a-r)^2]^{1/2}\}. \tag{11c}$$

In inverting (8), the following integral is used:

$$\int_0^\infty \cos(b\lambda) J_0(a\lambda)\,\mathrm{d}\lambda = H(|a|-|b|)\frac{1}{(a^2-b^2)^{1/2}}.$$

The condition where the argument of the step function σ becomes zero can be readily shown to be identical to

$$[x-\xi-U_\infty(t-\tau)]^2+(a-r)^2 = [a_\infty(t-\tau)]^2.$$

This represents a front of a wavelet just passing an observation point (x, r) at time t (see figure 5); it originates at time τ from a source point S located at ξ on $r = a$, and is convected downstream in the x-direction with velocity U_∞, while its radius is simultaneously increasing at a speed a_∞. The shape of the front is circular in the (x, r)-plane. Obviously, the zone of influence for any wavelet is inside its circular front; outside is its zone of silence. For a fixed observation point P and a fixed source point S, then, there are two values of τ corresponding to two such limiting wavelets passing P at a given time t (figure 6): they are τ_1 and τ_2 given in (11*b*) and (11*c*).

1 corresponds to the wavelet front, originated at time τ_1 and whose receding side intersects P at time t, while 2 corresponds to the one whose advancing side intersects P.

Only those wavelets emitted during the time interval $\tau_1 < \tau < \tau_2$ affect P at time t, which corresponds to the condition $\sigma \geqslant 0$. Therefore, by replacing the integration limits for the second integral of (10) by τ_1 and τ_2, H may be dropped and (10) becomes

$$\phi' = \frac{U_\infty}{\pi m}\left(\frac{a}{r}\right)^{1/2} \int_0^{x-\bar{x}} \mathrm{d}\xi \int_{\tau_1}^{\tau_2} f(\xi,\tau) \frac{1}{[(\tau-\tau_1)(\tau_2-\tau)]^{1/2}} \mathrm{d}\tau. \tag{12}$$

It is convenient to rewrite this, by integration by parts, as

$$\phi' = \frac{U_\infty}{\pi m}\left(\frac{a}{r}\right)^{1/2} \left\{\frac{\pi}{2}\int_0^{x-x} [f(\xi,\tau_2)+f(\xi,\tau_1)]\,\mathrm{d}\xi - \int_0^{x-\bar{x}} \mathrm{d}\xi \int_{\tau_1}^{\tau_2} \frac{\partial f(\xi,\tau)}{\partial \tau} \arcsin\left(\frac{\tau-\frac{1}{2}(\tau_1+\tau_2)}{\frac{1}{2}(\tau_2-\tau_1)}\right)\mathrm{d}\tau\right\}, \tag{13}$$

where arcsin is the inverse sine function.

By taking the derivative with respect to x, we obtain

$$\frac{\partial}{\partial x}\phi' = \frac{U_\infty}{\pi m}\left(\frac{a}{r}\right)^{1/2} \left\{\pi f(x-\bar{x},t-\bar{t}) + \frac{\pi}{2}\int_0^{x-\bar{x}} \left[\frac{\partial f(\xi,\tau_2)}{\partial x}+\frac{\partial f(\xi,\tau_1)}{\partial x}\right]\mathrm{d}\xi - \int_0^{x-\bar{x}} \mathrm{d}\xi \frac{\partial}{\partial x}\left[\int_{\tau_1}^{\tau_2} \frac{\partial f(\xi,\tau)}{\partial \tau} \arcsin\left(\frac{\tau-\frac{1}{2}(\tau_1+\tau_2)}{\frac{1}{2}(\tau_2-\tau_1)}\right)\right]\mathrm{d}\tau\right\}, \tag{14}$$

where

$$\bar{t} = \frac{1}{a_\infty m} M_\infty (a-r). \tag{15}$$

As shown in figure 4, $x-\bar{x}$ is the source point Q, corresponding to the intersection of the left-running Mach wave passing $P(x,r)$ with $r=a$; $\bar{t}$ corresponds to the time required for the wavefront of the signal, which originates from Q and propagates along the Mach wave, to reach P.

2.2. *Near-shock approximation*

Consider points near the leading Mach wave corresponding to

$$x-\bar{x} \approx 0. \tag{16}$$

Then, the second and third integrals in the brackets of (14) become negligible and one obtains

$$\frac{\partial}{\partial x}\phi' \approx \frac{U_\infty}{m}\left(\frac{a}{r}\right)^{1/2} f(x-\bar{x},t-\bar{t}). \tag{17}$$

Similarly, the radial component of the velocity may be written approximately as

$$\frac{\partial}{\partial r}\phi' \approx U_\infty \left(\frac{a}{r}\right)^{1/2} f(x-\bar{x},t-\bar{t}). \tag{18}$$

From (17) and (18), the component of the velocity normal to the leading Mach wave may be obtained as

$$u'_{n,2} \approx \frac{M_\infty}{m} U_\infty \left(\frac{a}{r}\right)^{1/2} f(x-\bar{x},t-\bar{t}), \tag{19}$$

where the subscript 2 denotes, for future reference, the downstream region of the leading Mach wave (see figure 4). The corresponding velocity component tangent to the leading Mach wave is given by

$$u'_{t,2} \approx 0. \tag{20}$$

The corresponding expression for $(\partial/\partial t)\phi'$ is

$$\frac{\partial}{\partial t}\phi' \approx 0. \tag{21}$$

This shows that for points near $x-\bar{x} \approx 0$, the flow field is quasi-steady. Physically, this is due to the fact that near the leading Mach wave, the characteristic length scale is $x-\bar{x}$. Thus the reduced frequency based on $x-\bar{x}$ can become as small as one wants (Kurosaka 1974). Finally, the corresponding expression for the perturbed pressure is derived as

$$p' \approx -\rho_\infty \frac{U_\infty^2}{m}\left(\frac{a}{r}\right)^{1/2} f(x-\bar{x},\, t-\bar{t}). \tag{22}$$

From this, and recalling that our objective is to examine the influence of vortices, which is of course characterized by a pressure drop, we now take f, initially specified as an arbitrary radial component of the velocity, to be positive:

$$f > 0. \tag{23}$$

2.3. *Shock movement and total temperature change*

As shown in figure 3, we denote the region upstream of the leading oblique shock by region 1 and downstream by region 2. Take the coordinate system where the shock becomes normal. In the undisturbed state, the velocity components normal to the shock are $u_{n,1}$ and $u_{n,2}$. They are related by

$$\frac{u_{n,1}}{u_{n,2}} = \frac{(\gamma+1)M_{n,1}^2}{(\gamma+1)M_{n,1}^2+2}, \tag{24}$$

where $M_{n,1} = M_\infty \sin\beta_s$, β_s being the shock angle.

With the condition in region 1 fixed, when a disturbance $u'_{n,2}$ is added in region 2, the shock starts to move in such a way that in the moving-shock coordinate, the corresponding form of (24) applies. Upon linearization and combined with (19), the shock velocity normal to the undisturbed shock, u'_s, which is taken to be positive in the downstream direction, becomes

$$u'_s = \frac{(\gamma+1)M_{n,1}^2}{2(1+M_{n,1}^2)}\frac{M_\infty U_\infty}{m}\left(\frac{a}{r}\right)^{1/2} f(x-\bar{x},\, t-\bar{t}). \tag{25}$$

(It is also equal to Ψ_t, where Ψ is the displacement of the shock measured normal to its steady position and taken to be positive in the downstream direction. Strictly speaking, in relating u'_s to f, we have to consider the local slope of the displaced shock, Ψ_σ, where σ is the distance measured along the steady shock. A detailed analysis shows, however, that in order to determine Ψ_σ, one needs the velocity potential corresponding to $O(\epsilon\theta_0)$. In view of this complexity, here we neglect Ψ_σ.)

We next consider the total temperatures on both sides of the shock defined as

$$T_{t,1} = T_1 + \frac{1}{2c_p}(u_{n,1}^2 + u_{t,1}^2), \tag{26}$$

and $$T_{t,2} = T_2 + T_2' + \frac{1}{2c_p}[(u_{n,1} + u_{n,2}')^2 + (u_{t,2} + u_{t,2}')^2]. \tag{27}$$

In the shock-coordinate system, corresponding total temperatures on both sides of the shock are equal; using this and upon linearization, combined with $u_{t,1} = u_{t,2}$, (20), (24) and (25), we obtain an expression for the difference in the total temperatures:

$$c_p \Delta T_t = -u_{n,1} \frac{(M_{n,1}^2 - 1)}{(M_{n,1}^2 + 1)} \frac{M_\infty U_\infty}{m} \left(\frac{a}{r}\right)^{1/2} f(x - \bar{x}, t - \bar{t}), \tag{28}$$

where $$\Delta T_t = T_{t,2} - T_{t,1}, \quad u_{n,1} = U_\infty \sin \beta_s.$$

This, together with (23) and (25), is our central result.

2.4. *Postulate for shock movement*

The application of the foregoing results to the present problem calls for considerations such as (i) the azimuthal characterization of the vortical structures around the jet periphery, which in the analysis is assumed to be axisymmetric, and (ii) the formative development of the vortical structures and their interaction with shocks.

First, regarding the presence of large-scale structures even in supersonic jets, Lepicovsky *et al.* (1986) visually observed the convected movement of large-scale structures along the periphery of a jet at Mach number 1.4; in order to capture large-scale structures, not only did Lepicovsky *et al.* acoustically excite the jet, but they also resorted to a unique laser-schlieren system utilizing a time-delayed trigger and photographic ensemble-averaging technique. Although the presence of large-scale structures in supersonic jets was definitively confirmed, such additional details of the large-scale structures as their azimuthal feature are unfortunately not available.

In connection with this issue of the azimuthal dependence, theoretical studies have been conducted mostly in the context of supersonic jet noise, where the spatial evolution of axisymmetric and asymmetric modes is examined (Tam & Burton 1984; Ahuja *et al.* 1992). In particular, Ahuja *et al.* show that the asymmetrical or helical modes become most dominant for jet Mach numbers over 1.3 (for a recent comprehensive review and bibliography of these and related topics, see Tam 1991).

Seiner, Manning & Ponton (1986) addressed this question of azimuthal modes experimentally for an axisymmetric convergent–divergent nozzle designed for a Mach number of 2. Both from acoustic measurements and schlieren records of shock-cell movement, they deduced that at a lower Mach number of 1.56, the mode was indeed of the flapping type: a superposition of two equal but oppositely directed helical modes. At the higher Mach number of 1.8, however, schlieren records could not determine the preferred azimuthal structure, but from acoustic measurements this indeterminacy was found to be due to the coexistence of axisymmetric and helical modes. As the design Mach number was approached, axisymmetric modes became increasingly important. A similar dominance of axisymmetric modes over the helical modes at the design point was also found from acoustic measurements by Troutt & McLaughlin (1982) for an axisymmetric supersonic nozzle designed for a Mach number of 2.1, and by Suda, Manning & Kaji (1993) for a rectangular nozzle designed for a Mach number of 1.8.

Therefore it appears that even in supersonic jets the large-scale structures are indeed of the axisymmetric or vortex-ring type so long as the jets are operating near the design Mach number; this is the condition to which the foregoing analysis of linearized analysis is applicable. Let us then proceed to consider the formation process of the vortex rings and their interaction with shocks.

First, when the vorticity in the nozzle boundary layer starts to roll up and a vortex ring is initially formed at point A near the leading shock (see figure 3), the pressure at the vortex core starts to drop, and therefore f of equation (23) starts to increase from zero. Thus the shock starts to deviate from the 'steady condition', swinging in the downstream direction (β_s of figure 3 decreases), and the total temperature decreases across the shock; the magnitude of the drop increases, according to equation (28), like $1/r^{1/2}$ towards the jet centre. The latter is caused by the focusing effect of the leading disturbances convergingly beaming towards the duct centre, which increases the velocity of the shock movement there (although the singular behaviour at $r = 0$ is an apparent one associated with the asymptotic representation used in §2.1).

As the vortex is convected in the downstream direction, it grows in size and its strength increases owing to the continuous supply of vorticity from the boundary layer; the pressure at its centre drops correspondingly. In response, the shock continues to swing in the downstream direction (β_s of figure 3 decreases further), with its root attached to the nozzle lip.

Naturally, this process continues only up to a certain point. When the vortex gains sufficient strength, the radially inward penetration of entrained ambient fluid induces an effect equivalent to the injection of a secondary fluid into the main supersonic stream; in that case, an oblique shock appears upstream of the injection. Here, similarly, the entrainment causes a re-emergence of the leading-edge shock along the 'steady' position; at the same time, the entrainment serves to sever (from the nozzle lip) the preceding shock, which has been swept in the downstream direction. The latter now starts to move with the travelling vortices. (Recently Suda *et al.* 1993 also detected a similar downstream travel of the shocks corresponding to the third cell at a lower pressure ratio. This observation was made possible by their use of an ultra-high-speed camera combined with their particular choice of a plane jet; for a two-dimensional jet, the shock movement is visually enhanced by two-dimensional overlapping, while for axisymmetric jets, the lack of overlapping due to three-dimensionality would obscure the details of such movement.)

After the re-emergence of the leading-edge shock, the process repeats itself. Although the temporal increase of static pressure associated with the re-emergence would induce instantaneous hot spots along the leading edge of the new shock, this would occur only for a short period, when compared to the longer time scale associated with the downstream motion of the shock. Thus as a time-average, the cooling phase associated with the downstream movement of the shock dominates.

If the above hypothesis is tenable, the decrease in time-averaged T_t should appear only downstream of the steady position of the leading-edge shock. Thus when we plot the radial profiles of time-averaged T_t at a fixed x-location (say, starting from point Q of figure 4 and moving radially inward), the departure of T_t from its upstream value should be present only in the annular region between Q and B. From B to the centreline, T_t should retain its upstream value. Furthermore, as the downstream distance x increases, the region where T_t decreases from its upstream value should progressively move inward; finally at point C, such a region reaches the jet centre. The experimental data to be presented in §3 confirm these expectations.

It should be pointed out that the presumed appearance of the decreased region of T_t without any presence of the increased region of T_t does not violate the conservation of the flux of T_t, for the latter is always satisfied for a material body of the air, when viewed from the shock coordinate system.

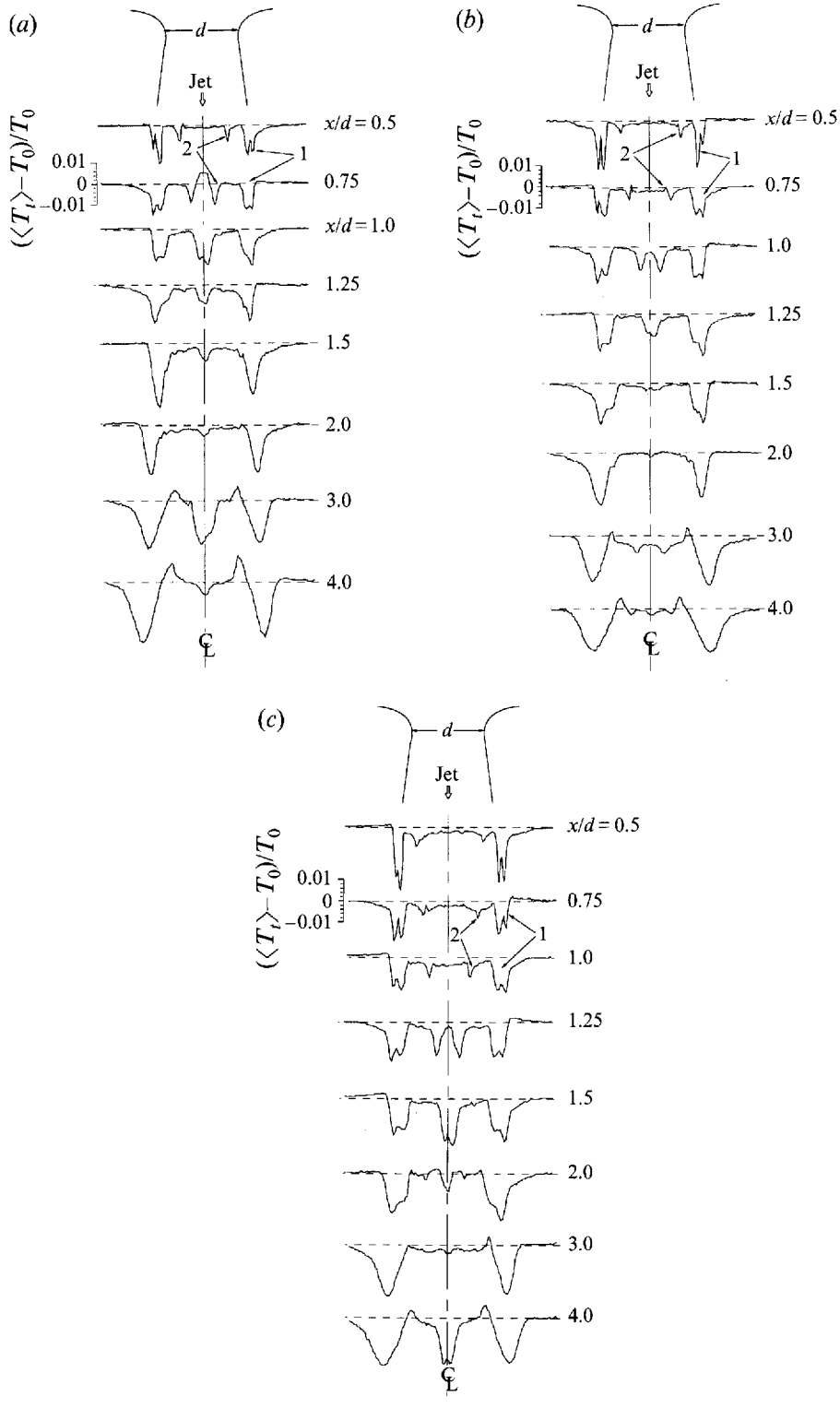

FIGURE 7. Radial profiles of the total temperature for overexpanded jets. (*a*) $P_0/P_a = 5.08$, (*b*) $P_0/P_a = 6.44$, (*c*) $P_0/P_a = 7.82$.

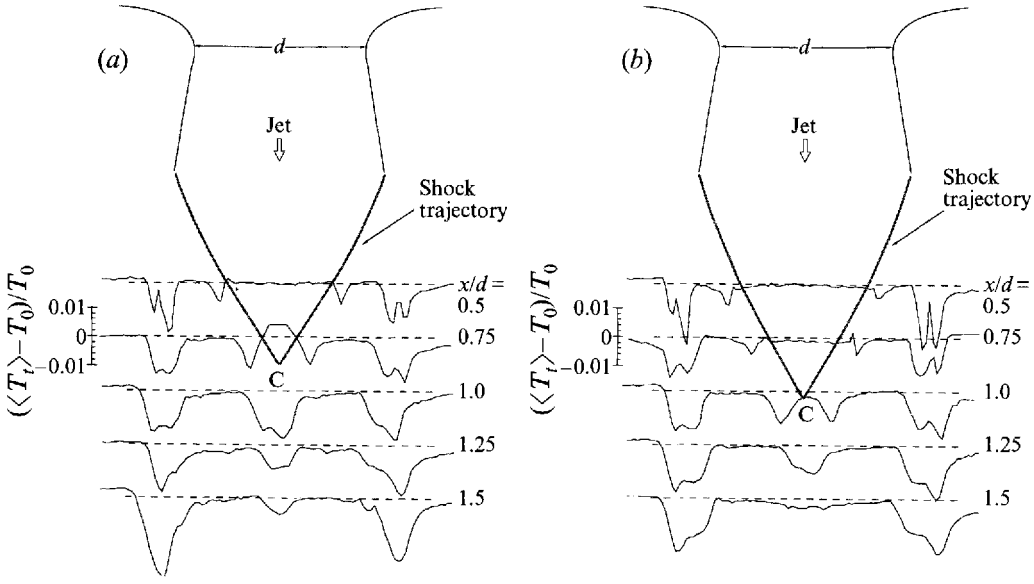

FIGURE 8. Radial profiles of the total temperature for an overexpanded jet, drawn to scale, with the shock trajectory drawn for reference. (*a*) $P_0/P_a = 5.08$, (*b*) $P_0/P_a = 6.44$.

3. Measured $\langle T_t \rangle$ profiles for overexpanded free jets

In the light of the results of the foregoing model analysis, experiments were carried out to obtain the total temperature profiles of a free jet emanating from a convergent–divergent nozzle.

Utilizing the air jet facility described in Part 1, the time-averaged total temperature $\langle T_t \rangle$ distribution in an overexpanded free jet was measured by traversing a United Sensor YCT-156 probe across the jet flow field. The probe has a spatial resolution estimated to be 0.025 cm. A Macintosh computer controls the probe position to an accuracy of 0.005 cm, and reads the temperature. A circular nozzle with a throat diameter of 2.54 cm was used for the tests; with an exhaust-to-throat area ratio of 1.69, it was designed for ideal expansion at a Mach number of 2, which corresponds to $P_0/P_a = 7.82$. During the tests, as stated before, the total temperature of the jet as measured in the upstream settling chamber is held constant and equal to the ambient temperature of $T_a = 21$ °C (for other details, see Fox 1994).

The results are presented in figure 7, where the radial profiles of $\langle T_t \rangle$ distributions are plotted at different downstream locations, x/d (where d is the throat diameter) and three pressure ratios: (*a*) $P_0/P_a = 5.08$, (*b*) $P_0/P_a = 6.44$, and (*c*) $P_0/P_a = 7.82$, the design condition. The last condition is close to the upper limit of the experimental rig and therefore no attempt was made to obtain the under-expanded jet data for a convergent–divergent nozzle. The pressure ratios of figures 7(*a*) and 7(*b*), corresponding to overexpanded jets, are high enough to avoid the occurrence of shock-induced flow separation within the nozzle (e.g. Summerfield, Foster & Swan 1954).

Their gross features are similar to those of figure 1(*b*), obtained for an underexpanded convergent nozzle. Valleys at the outer radial positions labelled 1 correspond to the cooling caused by the vortex-induced T_t separation of Part 1. In the near field, the secondary valleys at the smaller radial positions labelled 2 correspond to the cooling caused by the present shock-induced T_t separation. The heating, or peaks that accompanied the valleys 1 of vortex-induced T_t separation (see Part 1) is cancelled out, in this time average, by the presence of valleys 2.

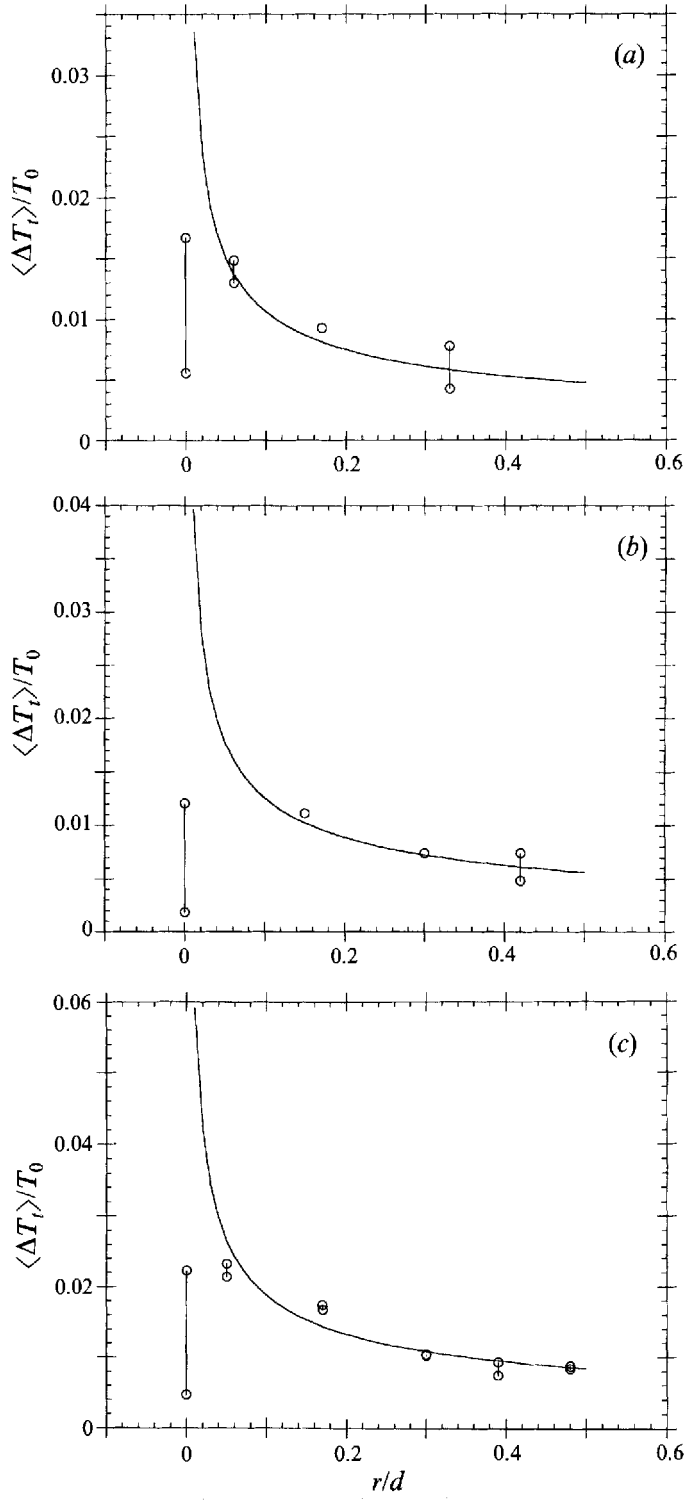

FIGURE 9. Maximum cooling in the radial temperature profile *vs.* r/d. (*a*) $P_0/P_a = 5.08$, (*b*) $P_0/P_a = 6.44$, (*c*) $P_0/P_a = 7.82$.

As the downstream distance x increases, valleys 1 move radially outward as expected for vortex-induced T_t separation. When compared to their subsonic counterpart (Part 1; O'Callaghan & Kurosaka 1993) the radial movement is slower owing to the slow enlargement of the outer edge of overexpanded jets. On the other hand, valleys 2 move progressively inward and eventually reach the jet centre, while the amount of cooling increases in a manner qualitatively consistent with the results of §2. When the valleys of T_t have coalesced at the centre, their values reach local minima at $x/d = 1$ for (*a*), $x/d = 1.25$ for (*b*), and $x/d = 1.5$ for (*c*) (there the cooling has reached local maxima).

The cooling then decreases as x/d increases but a second local minimum of T_t appears again at the centre at $x/d = 3$ for (*a*) and (*b*), and at $x/d = 4$ at (*c*). After this, the cooling starts to decrease once again. The reason why valleys 2 do not extend to the edge of the jet is, as mentioned just before, due to the cancelling effect of vortex-induced heating near the edge. (As already mentioned in §2, the predominant presence of cooling, which does not accompany much heating, does not violate the conservation of the flux of T_t, since a compensating adjustment by the density serves to conserve the flux.) The profiles were obtained by traversing the probe from left to right and the data seem to show an acceptable degree of radial symmetry.

In what follows, we make a more detailed comparison. Figure 8 shows the details of the $\langle T_t \rangle$ profiles in the near field. The shaded lines emanating from the nozzle lips are calculated shock trajectories at 'steady' conditions. These are obtained by constructing, for the given nozzle geometry, the expansion fans by the method of characteristics for axisymmetric flows, and then calculating the shock trajectories by shock–expansion fan interaction; the shock is treated as locally planar and boundary layer corrections are not applied for the nozzle. Note that (*a*) all of the shock-induced T_t valleys are located radially outboard of the shock trajectories, (*b*) the shocks approximately intersect the radially innermost edges of the valleys of shock-induced cooling, and (*c*) the valleys coalesce at the jet centre slightly downstream of the shock-convergence point C, as expected. This feature appears to lend support to the hypothesis stated in §2. (The cause of the heating in a narrow region inboard of the shock-induced cooling, which is seen only at $x/d = 0.75$ of case (*a*) and not elsewhere, is unknown.) The case shown in figure 7(*c*), which corresponds to the design condition, is obviously not amenable to such shock calculation and the observed persistence of shock-induced cooling for this case is considered to be due to the effect of the boundary layer and nozzle imperfections.

Figure 9 shows the amount of shock-induced cooling, $\Delta\langle T_t \rangle$, corresponding to the difference between T_0 and the lowest $\langle T_t \rangle$ of valleys 2 for various x/d, plotted against their radial position r. Also plotted are the theoretical curves corresponding to $\Delta\langle T_t \rangle \propto 1/r^{1/2}$ obtained in §2, where their bases are taken to be the measured $\Delta\langle T_t \rangle$ at $x/d = 0.5$. (Note that in figure 9, the absolute values of $\Delta\langle T_t \rangle$ are shown.) The agreement in trends appears to be favourable except at $r = 0$, which is of course an apparent singular point of the analytical expression.

From the spatial periodicity of the shock pattern combined with the $1/r^{1/2}$ behaviour, one would also expect the following: the second minimum of T_t at the jet centre mentioned in connection with the data of figure 7 (e.g. at $x/d = 3.0$ for figure 7*a*) should correspond to the second intersection of the shocks at the jet centre, the point E of figure 3; here the shocks are the reflection of the leading-edge shocks at the jet boundary. The distance from the nozzle to such a point E in the middle of the second cell may be equal to approximately three times the distance to the intersection of the leading-edge shocks (point C of figure 8). For figure 7(*a*), point C corresponds to $x/d = 0.9$; point E would therefore be about 2.7, which is in fact close to the

previously noted position of the second minimum, $x/d = 3.0$. (In details, point E of figure 3 is the intersection of the expansion fans, D–F, with the jet centre, where D–F is the reflection of the leading-edge shock with the jet boundary. As the vortex is being formed at A, β_s of the leading-edge shock A–D decreases, and the Mach number in region 2 is reduced. Correspondingly, the Mach number in region 3 drops twice as much and this reduction causes the angle of the expansion fans, γ_e, to increase. This results in a reduction of T_t.)

Further downstream (e.g. $x/d = 4$ for figure 7*a*), the amount of shock-induced cooling at the jet centre is reduced and at the same time twin peaks of heating appear to flank them. This heating corresponds to the class C particle of a subsonic jet, discussed in Part 1; a single hump that would normally be present at the jet centre in a purely subsonic jet (figure 1 *a*) is eroded into twin peaks by the shock-induced cooling, which took place upstream.

4. Remarks on underexpanded jets

In §1, we introduced our present topic by showing in figure 1(*b*) the results of underexpanded jets discharging from a convergent nozzle. If we now return to those results and compare them with the results for overexpanded jets from a convergent–divergent nozzle, presented in the preceding section as figure 7, the two are recognizably similar. This may not be so surprising because even in underexpanded jets, expansion waves which originally emanate from the nozzle lip reflect from the jet boundary as compression waves which coalesce into 'intercepting' shocks. These shocks, though their roots are not anchored at the nozzle lip, are also expected to generate shock-induced T_t separation. More detailed quantitative investigation such as comparison with the analysis is beyond the scope of the present study.

5. Conclusions

Motivated by initially perplexing data obtained for a supersonic free jet, we have shown that unsteady interaction between shocks and vortical structures formed around the jet periphery can generate supersonic cooling. This shock-induced cooling is distinctly different from that previously observed for a subsonic jet: vortex-induced cooling. For a supersonic jet, the latter is found to coexist, and in some regions, compete with the former. A model problem for shock-induced cooling is formulated and analysed for overexpanded jets emanating from a convergent–divergent nozzle. Its results appear to compare favourably with the experimental data, supporting the proposed mechanism that the cooling is caused by the shock movement induced by the formation and convection of vortices: the bias towards a net effect of cooling is essentially a reflection of the fact that the growth and movement of the vortices take place in the downstream direction only.

When an impingement plate is inserted, the shock-induced cooling would manifest itself as wall cooling, whose magnitude is significantly larger than the subsonic counterpart of Part 1 (Fox 1994). The shock-induced cooling is not limited to jets and it would occur whenever a shock is influenced by vortical structures. (The preliminary results for impinging supersonic jets, together with the earlier versions of free jet data accompanied by CFD results, were presented previously at the Symposium on Heat Transfer in Turbomachinery, Marathon, Greece, 1992.)

The authors wish to express their gratitude to an anonymous referee for his constructive criticism and providing pertinent references, and Professor Ahuja for informing us of additional references. The financial support by AFOSR under contract number F49620-88-0041 is greatly appreciated.

REFERENCES

AHUJA, K. K., MASSEY, K. C., FLEMING, A. J., TAM, C. K. W. & JONES, R. R. 1992 AEDEC-TR-91-20, AD-A245 463, Arnold Engineering Development Center, Arnold Air Force Base, Tennessee, Air Force Systems Command, US Air Force.

CARRIER, G. F. 1949 *J. Aero. Sci.* **16**, 150–152.

ÉRDELYI, A. (Ed.) 1954 *Tables of Integral Transforms*, vol. 1, p. 250. McGraw-Hill.

FOX, M. D. 1994 The effect of large-scale vortical structures on the heat transfer from a surface. PhD dissertation, Department of Aeronautics and Astronautics, University of Washington, Seattle, Washington, USA.

FOX, M. D., KUROSAKA, M., HEDGES, L. & HIRANO, K. 1993 *J. Fluid Mech.* **255**, 447–472 (and corrigendum, **261**, 1944, 376).

KUROSAKA, M. 1974 *J. Fluid Mech.* **62**, 811–827.

KUROSAKA, M. 1977 *J. Fluid Mech.* **83**, 751–773.

KUROSAKA, M., GERTZ, J. B., GRAHAM, J. E., GOODMAN, J. R., SUNDARAM, P., RINER, W. C., KURODA, H. & HANKEY, W. L. 1987 *J. Fluid Mech.* **178**, 1–29.

LEPICOVSKY, J., AHUJA, K. K., BROWN, W. H. & BURRIN, R. H. 1986 *AIAA Paper* 86-1941.

NG, W. F., CHAKROUN, W. M. & KUROSAKA, M. 1990 *Phys. Fluids* A **2**, 971–978.

O'CALLAGHAN, J. J. & KUROSAKA, M. 1993 *AIAA J.* **31**, 1157–1159.

SEINER, J. M., MANNING, J. C. & PONTON, M. K. 1986 *AIAA Paper* 86-1942.

SUDA, H., MANNING, T. A. & KAJI, S. 1993 *AIAA Paper* 93-4323.

SUMMERFIELD, M., FOSTER, C. R. & SWAN, W. C. 1954 *Jet Propulsion* **24**, 319–321.

TAM, C. K. W. 1991 In *Aeroacoustics of Flight Vehicles: Theory and Practice*. Vol. 1: *Noise Sources* (ed. H. H. Hubbard), chap. 6. NASA Reference Publication 1258, Vol. 1: WRDC Technical Report 90-3052.

TAM, C. K. W. & BURTON, D. E. 1984 *J. Fluid Mech.* **138**, 273–295.

TROUTT, T. R. & MCLAUGHLIN, D. K. 1982 *J. Fluid Mech.* **116**, 123–156.